Electrochimica Acta 158 (2015) 175–186

Contents lists available at ScienceDirect

Electrochimica Acta

journal homepage: www.elsevier.com/locate/electacta

Lattice Boltzmann Pore-Scale Investigation of Coupled Physical-electrochemical Processes in C/Pt and Non-Precious Metal Cathode Catalyst Layers in Proton Exchange Membrane Fuel Cells

Li Chen [a,b], Gang Wu [c,1], Edward F Holby [d], Piotr Zelenay [c], Wen-Quan Tao [a], Qinjun Kang [b,*]

[a] Key Laboratory of Thermo-Fluid Science and Engineering of MOE, School of Energy and Power Engineering, Xi'an Jiaotong University, Xi'an, Shaanxi 710049, China
[b] Earth and Environmental Sciences Division, Los Alamos National Laboratory, Los Alamos, NM, USA
[c] Materials Physics & Applications Division, Los Alamos National Laboratory, Los Alamos, NM, USA
[d] Materials Science & Technology Division, Los Alamos National Laboratory, Los Alamos, NM, USA

ARTICLE INFO

Article history:
Received 3 December 2014
Received in revised form 16 January 2015
Accepted 22 January 2015
Available online 24 January 2015

Keywords:
Proton exchange membrane fuel cell
catalyst layer
non-precious metal catalyst
reactive transport
effective transport properties
Lattice Boltzmann method

ABSTRACT

High-resolution porous structures of catalyst layers (CLs) including non-precious metal catalysts (NPMCs) or Pt for proton exchange membrane fuel cells are reconstructed using the quartet structure generation set. The nanoscale structures are analyzed in terms of pore size distribution, specific surface area, and phase connectivity. Pore-scale simulation methods based on the lattice Boltzmann method are developed to predict the macroscopic transport properties in CLs. The non-uniform distribution of ionomer in CL generates more tortuous pathways for reactant transport, greatly reducing the effective diffusivity. The tortuosity of CLs is much higher than that adopted by the Bruggeman equation. Knudsen diffusion plays a significant role in oxygen diffusion and significantly reduces the effective diffusivity. Reactive transport inside the CLs is also investigated. Although the reactive surface area of the non-precious metal catalyst (NPMC) CL is much higher than that of the Pt CL, the oxygen reaction rate is lower in the NPMC CL due to the much lower reaction rate coefficient. Although pores of a few nanometers in size can increase the number of reactive sites in NPMC CLs, they contribute little to enhance the mass transport. Mesopores, which are a few tens of nanometers or larger in size, are shown to be required in order to increase the mass transport rate.

© 2015 Elsevier Ltd. All rights reserved.

1. Introduction

Proton exchange membrane fuel cells (PEMFCs) are of great technological interest for vehicular and stationary power applications. Several technical barriers must be overcome before widespread commercialization of PEMFC technology. These barriers include high cost, material durability and water and heat management [1]. The utilization of precious metal-based catalysts, particularly platinum (Pt), contributes significantly to the cost of PEMFCs. Most of the utilized Pt catalyst is loaded at the cathode side due to the inherently sluggish oxygen reduction reaction (ORR) in the cathode catalyst layer (CCL). ORR reaction kinetics on the CCL have been shown to be five orders of magnitude slower than that of the hydrogen oxidation reaction (HOR) in the anode CL [2]. Cost reduction can be realized by optimizing CL design to enhance Pt utilization and thus to reduce Pt loading [3]. The limited availability and increased demand for Pt, however, is likely to raise the price of Pt [4]. An alternative to using Pt-based CLs is to develop active, selective, and durable non-precious metal catalysts (NPMCs) based on earth-abundant materials [3,5–15].

Different approaches have been proposed to develop different NPMC materials for ORR [5]. To date, the most promising NPMCs are a class of pyrolyzed transition metal nitrogen-carbon (M-N-C) complexes [5], which are obtained via heat-treatment of precursors including elemental transition ions, carbon and nitrogen [5,6]. For example, for the Polyaniline-FeCo-C (PANI-FeCo-C) NPMC developed by Wu et al. [11], the precursors are Ketjenblack, aniline oligomer, and cobalt nitrate and/or iron chloride. To replace Pt, the activity, selectivity, and durability of the NPMCs need to be improved [5]. The volumetric activity of an NPMC is the product of the active site density and the single-site activity [16]. With

* Corresponding author.
[1] Department of Chemical and Biological Engineering, University at Buffalo, The State University of New York, Buffalo, New York 14260.

http://dx.doi.org/10.1016/j.electacta.2015.01.121
0013-4686/© 2015 Elsevier Ltd. All rights reserved.

extensive efforts, NPMC volumetric activity has been improved significantly by deliberately selecting synthesis techniques [8,9]. However, the volumetric activity is measured under relatively high potential (0.8 V vs RHE (Reversible hydrogen electrode)), under which the dominant limiting factor is the electro-catalytic process. When fuel cells operate at low potentials (high current densities), transport limitations play a significant role in controlling ORR reaction rates. Therefore, NPMC activity and mass transport contributions must be combined in order to fully understand PEMFC performance [5]. To achieve higher activity, the thickness of NPMC CLs are usually ten times thicker than that of C/Pt CLs, leading to higher mass transport resistance in the NPMC CLs [6]. To date, many studies have focused on enhancing the NPMC activity with very little focus on the exacerbated mass transport issues [10]. Enhancing the transport efficiency inside the NPMC CL would lead to dramatic improvement in PEMFC performance but requires a more in depth understanding of the transport/structure relations in these CL systems.

Successful improvements of CLs are significantly dependent upon the fundamental understanding of the complex structures of CLs as well as the physicochemical reactions occurring in CLs. Typically, these structures contain nanometer scale features and can span many orders of magnitude in length making it extremely difficult to implement experimental investigations of in-situ reactive transport processes. Therefore, numerical simulations capable of spanning these length scales provide a promising method for gaining meaningful insights into the coupled electrochemical processes in a CL. Over the past two decades, numerical investigations of the Pt-based CL have progressed from ultra-thin interface models [17], to homogeneous models [18], to agglomerate models [19], and most recently to pore-scale models [20–28]. Each advancement corresponds to a higher resolution of the nanoscale porous structures at the cost of more complicated numerical models [19]. Pore-scale simulations, for instance, are based on explicitly resolving the realistic microstructures of porous media. Therefore, they do not require empirical relationships between statistic structural parameters and macro transport properties (such as porosity vs. effective diffusivity). Pore-scale simulations can be used to improve the fundamental understanding of reactive transport processes in porous media. The importance of pore-scale simulations is reflected in the increasing number of studies about pore-scale studies of reactive transport phenomena in Pt-based PEMFCs [20–36]. However, pore-scale studies related to NPMCs-based PEMFCs has not been reported.

The objective of the present study is to develop a pore-scale model based on the lattice Boltzmann method (LBM) for the coupled physic-electrochemical processes in both C/Pt and NPMC cathode CLs in PEMFCs. To the best of our knowledge, only Kim et al. [22] has adopted a LBM approach for transport processes in CL, however they did not consider the coupled electrochemical reactions. The present study applies a pore-scale model to CLs to evaluate the effects of nanoscale structural characteristics on the macroscopic transport properties, thus improving the fundamental understanding of reactive transport processes in the nanostructures of CLs. While there are a number of pore-scale studies of mass transport in Pt-based CLs [20–32], there is no such study on NPMC CLs. Our pore-scale model will be applied to the reactive transport processes in both Pt CLs and NPMC CLs, representing the first such study on NPMC CL systems. The rest of this paper is arranged as follows. In Section 2, the reconstruction processes of nanostructures of CLs are introduced. In Section 3, the physico-electrochemical model for reactive transport processes within the CLs is established. In Section 4, the numerical details of the LBM methodology are introduced. In Section 5, effects of CL morphology on the effective transport coefficients of oxygen and protons are investigated. The predicted effective transport coefficients are compared with results from the literature. Particular attention will be paid to differences between Pt and NPMC CLs and how those differences affect the reactive transport processes. Finally, conclusions are discussed in Section 6.

2. Reconstruction of nanostructures of the catalyst layers

The final nanostructures and performance of M-N-C catalysts are strongly affected by several factors including the type of precursors and synthesis conditions [11]. Therefore, we need to select a representative NPMC structure for this study. We have chosen the PANI-FeCo-C NPMC developed by Wu et al. [11]. The synthesis of this catalyst is as follows (also shown in Fig. 1). First, Ketjenblack, aniline oligomer and transition metal salts are mixed. Ammonium is added into the mixture to polymerize aniline. Then, the composite is dried and subjected to heat treatment in nitrogen in the temperature range of 400–1000 °C. The heat treated product is acid leached, after which a second heat treatment in nitrogen is implemented. The PANI-FeCo-C shows excellent performance, achieving a maximum power density of 0.55 W cm^{-2} at a cell voltage of 0.38 V (fuel cell voltage without correction of the voltage drop caused by membrane ionic resistance), and excellent performance retention after 700 h of potential hold at 0.4 V [11]. Fig. 2 shows a SEM of the nanoscale structures of PANI-FeCo-C with heat treatments of 900 °C [11], where formation of agglomerates with typical size of hundreds of nanometers can be seen.

The electrochemical reaction kinetics, structural morphology, and reactive site distributions of PANI-FeCo-C CLs are different from Pt CLs. First, Pt CLs are nanoscale porous media with random three-phase composites of pores, carbon-supported Pt (C/Pt), and ionomer (electrolyte). For the PANI-FeCo-C CL, the solid phase consists of carbon black, graphitic PANI, and metal aggregates. Second, in Pt CLs, ORR takes place on Pt particles surrounded by oxygen transporting void, electron conducting solid, and proton conducting ionomer phases. Together, these three phases constitute the triple-phase-boundary (TPB) [37,38]. The exact nature of the active ORR sites in NPMCs, however, is still under debate [11,39]. The doped nitrogen is likely critical to the active site formation [11]. Additionally, unlike in the Pt CL systems, there is no distinction between catalyst and the support in the considered NPMC as active sites are part of the support.

Although there are many differences between Pt CLs and NPMC CLs, we choose to focus on how reactive transport changes due to the different distribution of ORR active sites. Comparing SEMs of a NPMC CL in Fig. 2 with that of a Pt CL shown in Ref. [24] (Fig. 1 in Ref. [24]), it can be found that the porous structures of the two different catalysts are quite similar at the scale of hundreds of nanometers, showing formation of agglomerates with approximately equal size of primary particles. This observation leads to the assumption in the present work that the NPMC CL has the same solid structure as the Pt CL at the agglomerate scale. This assumption allows for direct comparison between localized active site distributions (Pt CL-like) and diffuse active site distributions (NPMC CL-like). The first step then is to generate the solid structure to be used for the comparative simulations.

The nanoscale topology of a CL can be achieved via computational reconstruction algorithms using experimental input from techniques such as SEM. In the literature, several reconstruction methods have been developed for Pt CLs including the Gaussian random field method proposed by Want et al. [20,21], the sphere-based annealing method by Kim and Pitsch [22], and the random carbon sphere method by Lange et al. [23,26,27]. Recently, Siddique and Liu [24] developed a reconstruction method based on the specific synthesis process used in fabricating a given CL structure. The computational

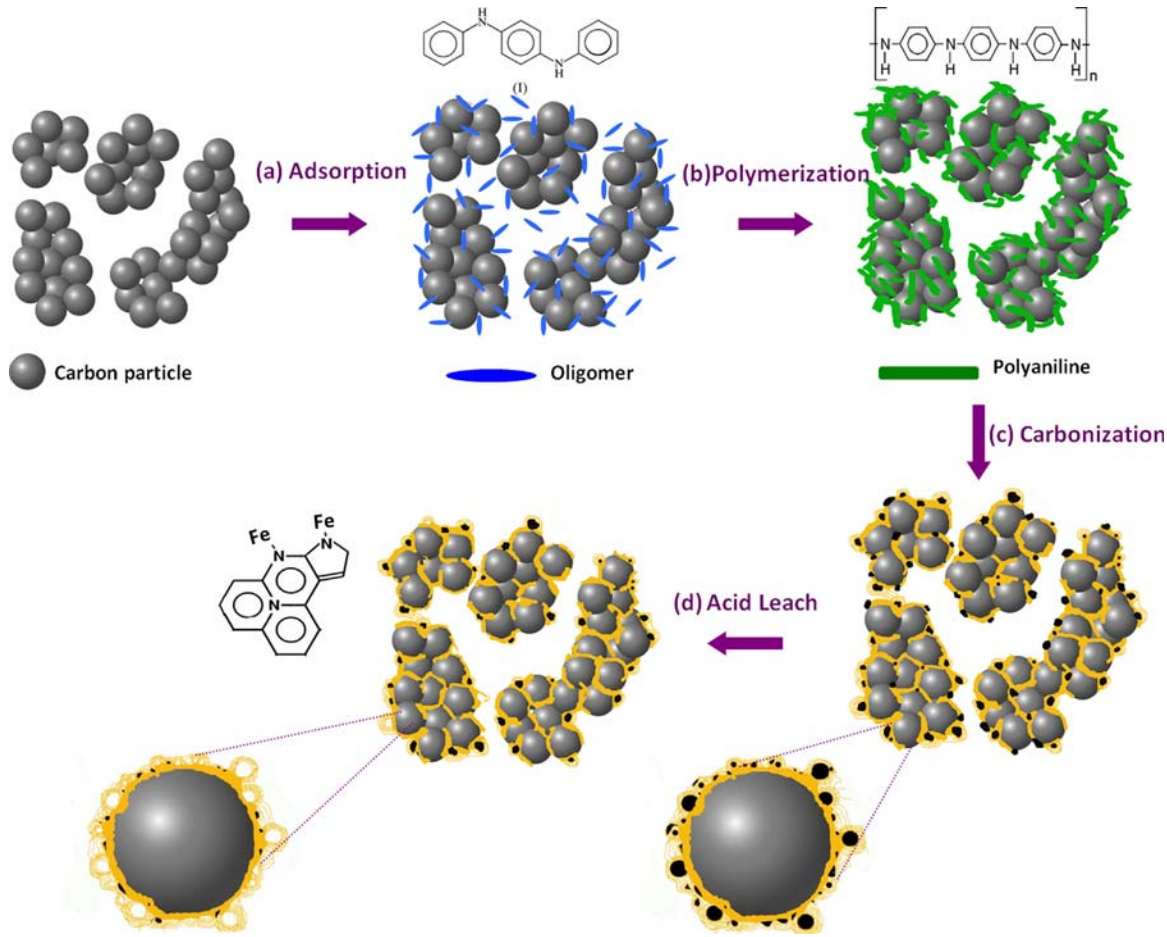

Fig. 1. Schematic diagram of the synthesis of PANI-M-C catalysts. (a) Mixing of high–surface area carbon with aniline oligomers and transition-metal precursor (M: Fe and/or Co). (b) Oxidative polymerization of aniline by addition of APS. (c) First heat treatment in N_2 atmosphere. (d) Acid leaching. The second heat treatment after acid leach is not shown. (Reprinted from Fig. 1 in Ref. [11]).

representation of the CL is reconstructed step by step based on experimental fabrication processes including carbon seed generation, carbon phase growth, Pt deposition, and ionomer inclusion.

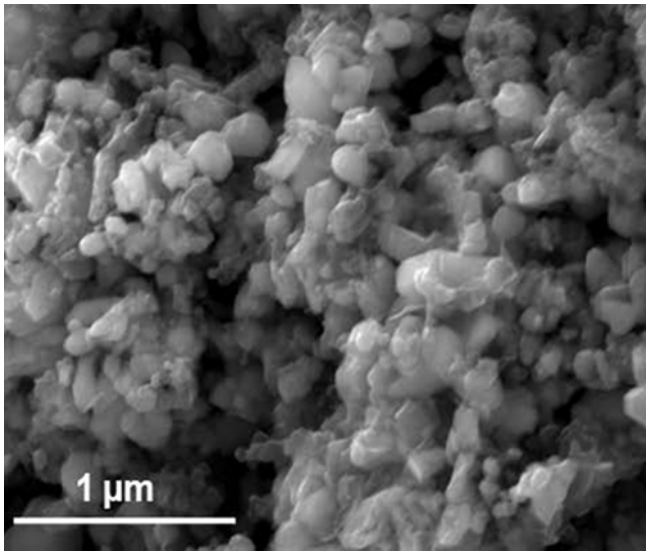

Fig. 2. SEM of the PANI-FeCo-C with heat treatment of 900 °C (Reproduced from Fig. S6 in Ref. [11]).

This method had a much higher resolution (~2 nm) which allows for a more detailed distribution of Pt particles when compared with previous studies [20–23,26,27,40]. In the present work, we follow this synthesis guided motivation.

2.1. Pt catalyst layer

Volume fractions for different components can be calculated based on the following design parameters of CL manufacturing [25]: (1) platinum loading (γ_{Pt}, mg cm^{-2}); (2) ionomer loading (β_N, weight ratio of ionomer to total electrode weight), (3) platinum to carbon weight ratio (θ_{Pt}).

$$\varepsilon_N = (1-\varepsilon)\frac{(1+\theta_{Pt})\beta_N/(\rho_N(1-\beta_N))}{\theta_{Pt}/\rho_{Pt} + 1/\rho_C + (1+\theta_{Pt})\beta_N/(\rho_N(1-\beta_N))} \tag{1a}$$

$$\varepsilon_C = (1-\varepsilon)\frac{1/\rho_C}{\theta_{Pt}/\rho_{Pt} + 1/\rho_C + (1+\theta_{Pt})\beta_N/(\rho_N(1-\beta_N))} \tag{1b}$$

$$\varepsilon_{Pt} = (1-\varepsilon)\frac{\theta_{Pt}/\rho_{Pt}}{\theta_{Pt}/\rho_{Pt} + 1/\rho_C + (1+\theta_{Pt})\beta_N/(\rho_N(1-\beta_N))} \tag{1c}$$

where ρ is density and subscripts "Pt", "C" and "N" represent platinum, carbon and ionomer, respectively. ε is the porosity, namely the volume fraction of void space. The platinum loading, γ_{Pt} (mg cm^{-2}), is related to ε_{Pt} by the following equation

$$\gamma_{Pt} = \varepsilon_{pt}\rho_{Pt}l \quad (2)$$

where l (cm) is the thickness of the CL. Having obtained the required volume fractions as a function of known input values from synthesis, we turn our attention to how these phases are distributed in the considered spatial domain via the adopted reconstruction methods.

2.1.1. Quartet structure generation set for generating carbon

Quartet structure generation set (QSGS) [41] is employed for carbon seed generation and carbon growth. It has been demonstrated to be capable of generating morphological features closely resembling those of many real porous media [41]. The QSGS procedures are briefly described as follows: (1) Randomly distribute carbon seeds in the domain based on a distribution probability, c_d, which is related to the volume fraction of carbon, ε_C. A random number between 0 and 1 is assigned to each computational cell in the domain. If the random number is less than or equal to c_d, the cell is selected as a carbon core. (2) Grow existing carbon seeds to neighboring cells. "Growth" (assignment of more carbon cells based on initial seeds) occurs via two assignment processes. By example, considering a given carbon seed cell A with a neighboring cell, $A\alpha$, which was not assigned as a carbon seed in step 1, carbon assignment proceeds by: a. if one of $A\alpha$'s neighboring cells other than A is also a carbon seed cell, $A\alpha$ is assigned as a carbon cell. Materials tend to bond with each others to reduce the surface energy [24] and this step leads to bridging of carbon seeds; b. Otherwise, $A\alpha$ is assigned as a carbon cell based on another probability $P\alpha$. In the present study, only the cells adjacent to carbon seeds are considered for growth, namely the six cells in directions (1,2,3,4,5,6), as shown in Fig. 3. For each direction, a new random number is generated, and if it is less than $P\alpha$ the neighboring cell in the α direction becomes a carbon phase cell. (3) Repeat (1) and (2) until the volume fraction of carbon phase is achieved.

There are three parameters (c_d, $P\alpha$,ε_C) controlling the generated morphologies of the carbon phase. c_d denotes the number density of the growing seeds of carbon in the CL. A higher value of c_d leads to more seeds in the system, resulting in more particles of carbon phase, while a lower value leads to less seeds, and thus, bigger carbon agglomerates. $P\alpha$ is the probability of the growth of an existing carbon cell towards its neighboring cell. In order to generate isotropic structures, $P\alpha$ of the six main directions (1,2,3,4,5,6) should be the same. Antistrophic structures can be obtained by setting different values for $P\alpha$ in different directions.

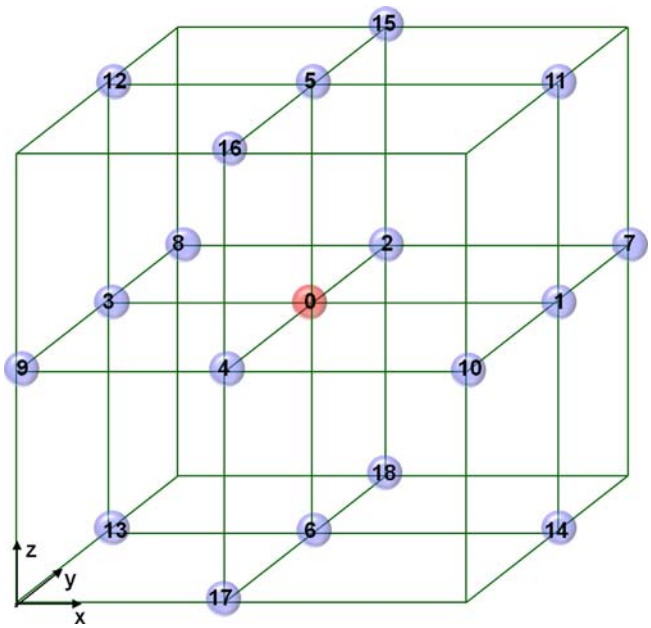

Fig. 3. 6 directions for growth in the QSGS or the D3Q19 lattice model in LBM.

2.1.2. Random dispersion of Pt particles

Transmission electron microscopy (TEM) shows that Pt particles are randomly distributed on the carbon surface [37]. The typical size of Pt nanoparticles usually is 2–5 nm [42]. Based on these experimental observations, Pt particles with a size of 5 nm, the resolution of a computational cell in the present nanoscale simulations, are randomly located on the QSGS generated carbon surface. A random number is assigned to each cell adjacent to the carbon phase in the domain. If the number assigned to a cell is less than a prescribed probability, the value of which is quite lower than the volume fraction of Pt, the cell is assigned as a Pt phase cell. This process is repeated until the volume fraction of Pt is achieved. With the above distribution scheme, generally, five faces of a cubic Pt cell are exposed to void or ionomer phase, while one face is in contact with the carbon support.

2.1.3. QSGS for generating ionomer

In the simplest case, the ionomer can be assumed to be a thin film uniformly covering the surface of the C/Pt structure. Most of the agglomerate models [19] and quite a few pore-scale models [22,23,26] were based on this scenario. Lange et al. [23,26,27] pointed out that uniform ionomer distribution may lead to overestimated effective oxygen diffusivity and underestimated proton conductivity [26]. When a nonuniform ionomer layer is presented, very narrow void spaces can be formed which act as barriers for reactant transport. In addition, nonuniformly distributed ionomer also tends to connect carbon spheres and thus can reduce the turtuosity and enhance proton conductivity [26]. In this work, the QSGS method is adopted to generate a nonuniform distribution of ionomer on the surface of C/Pt. The generation steps are similar to that in Section 2.1.1 for C generation. Note that the scheme introduced in Step 2a helps to establish connections between local ionomer cells.

In the present work, all the reconstructed Pt CL structures are based on the following parameters: $\beta_N = 0.3$, $\theta_{Pt} = 0.4$, $\rho_N = 2000$ mg cm^{-3}, $\rho_C = 1800$ mg cm^{-3}and $\rho_{Pt} = 21{,}450$ mg cm^{-3} [25]. We reconstruct different CL structures by changing the porosity, ε. Note that changing the porosity affects several other parameters including the volume fractions of carbon, Pt and ionomer; larger porosity leads to smaller volume fractions of carbon, Pt and ionomer. Fig. 4 shows generated 3D structures of a Pt CL using our reconstruction method with ε=0.4. Details of the structures will be discussed in Section 5.1.

2.2. Non-Precious metal catalyst layer

For the considered PANI-FeCo-C NPMC CL, PANI is employed as the source of nitrogen and carbon, which has several benefits. The similarity between the structures of PANI and graphite facilitates the incorporation of nitrogen-containing active sites into the partially graphitized carbon matrix during the heat treatment. Besides, using PANI can guarantee the uniform distributions of nitrogen sites on the surface of solid phase and thus an increase in active-site density [11]. Hence in the present work, for the PANI-FeCo-C CL, the C/Pt solid phase generated in Section 2.1 is considered as a mixture of carbon black, graphite PANI and metal aggregates in PANI-FeCo-C CL; and the active sites uniformly distribute on the entire solid surface, but with a much lower reaction rate coefficient compared with that of Pt [11].

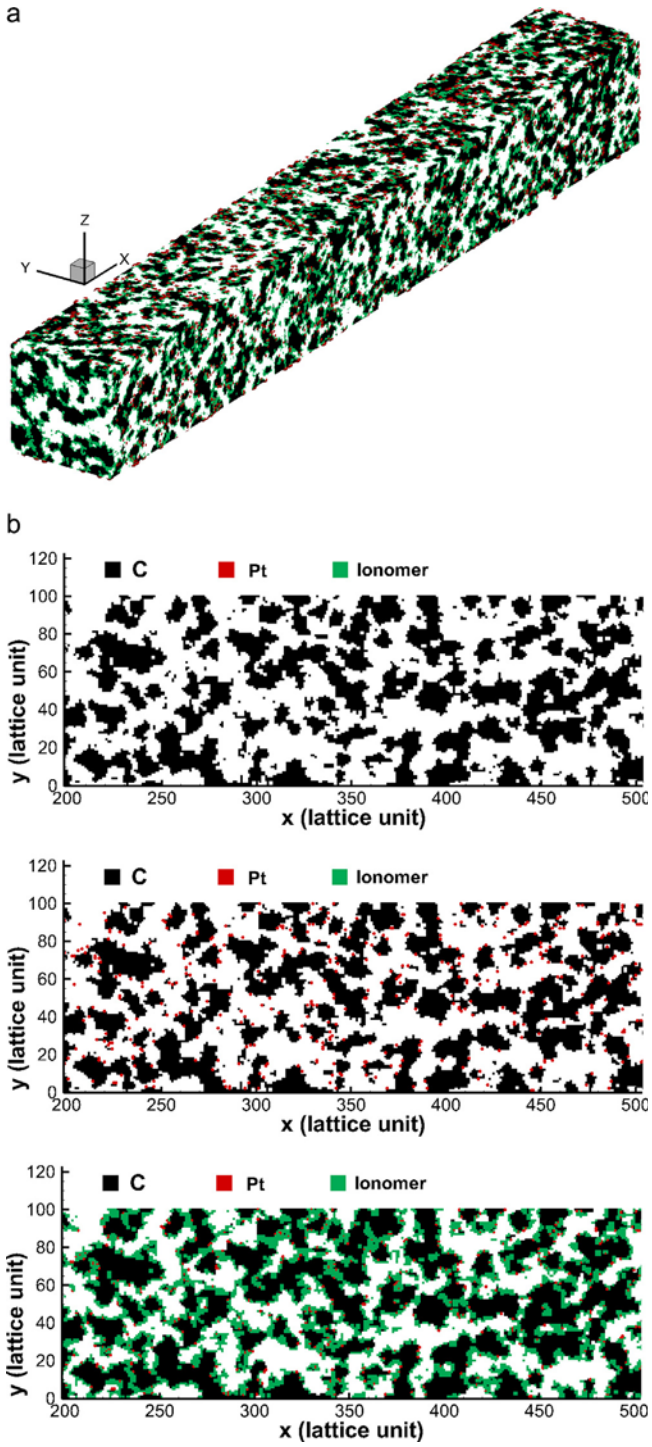

Fig. 4. Reconstructed nanoscale structures of CCL, (a) 3D structures; (b) Detailed distributions of carbon black (top), C/Pt (middle) and Nafion covered on C/Pt (bottom).

3. Physico-electrochemical model

3.1. Governing equations

The computational domain of the pore-scale simulated CL is reconstructed based on the methods in Section 2. The spatial coordinate x is defined so that the positive direction points from the gas diffusion layer (GDL)/CL interface to the CL/proton exchange membrane (PEM) interface, with its origin located at the GDL/CL interface. The coupled physico-electrochemical processes modeled are as follows: the oxygen diffusion from the GDL into the CL; the oxygen diffusion from pores into the ionomer; the diffusion of oxygen in the ionomer; the proton conduction in the ionomer; and the electrochemical ORR reactions on the active sites. The key assumptions employed in this model are as follow: a) Electron conduction limitations within the solid phase are neglected as the electronic conductivity is considered to be sufficiently high; b) the electric potential in the solid is assumed to be uniform [20]; c) Effects of water vapor and water-air two-phase flow are not considered [20,23]; d) Isothermal and steady state operation conditions are assumed; e) conductivity of protons in the ionomer is constant. Further details are available in Refs. [20,23,24,26,27,43–46].

The oxygen transport equation in pores is described by Eq. (3), where C is the concentration and D is the diffusivity. In the pores, diffusion mechanisms include bulk diffusion and Knudsen diffusion. Oxygen is transported to the active sites as a molecular species dissolved in the ionomer. The dissolved oxygen concentration at the pore-ionomer interface, $C_{O_2,e}$, is determined by Henry's law, as described by Eq. (4a) and (4b) with H as the Henry's coefficient. Eq. (5a) and (5b) describes the oxygen transport in ionomer, where S is the source term. As the concentration field is discontinuous at the pore-ionomer interface, Eqs. (3) and (5a) and (5b) an be solved in the pore and the ionomer phases, respectively, with Eq. (4a) and (4b) imposed at the interface. Another efficient way to solve such transport process with concentration jump at the phase interface is to combine Eqs. ((4a)–(5b)) to yield Eq. (6a) based on the isothermal condition. In this way instead of solving for the real concentration in the ionomer phase, a hypothetical concentration in the ionomer is solved. Therefore, a continuous C_{O_2} can be defined in the pore and ionomer as given by Eq. (6b) with D as D_{O_2} and $D_{O_2,e}$, and S as 0 and $S_{O_2,e}H/RT$ in pore and ionomer phase, respectively. After Eq. (6b) is solved, the actual oxygen concentration in the ionomer can be back-calculated using Eq. (4a) and (4b).

The governing equation for the proton transfer in the ionomer is given by Eq. (7), where σ is the proton conductivity and ϕ is the potential of the electrolyte phase. S_e is the source term related to electrochemical reaction. The ORR rate, i, is a function of local oxygen concentration and potential and is described by the Tafel equation, Eq. (8), where $C_{O_2,ref}$ is the reference oxygen concentration, α is the cathode transfer coefficient, F is Faraday's constant, and $i_{0,m}$ is the exchange current density. Note that in Eq. (8), ϕ_e is used, because $\eta = \varphi_s - E_{eq} - \varphi_e$ and solid phase potential ϕ_s and equilibrium potential E_{eq} are assumed to be constant in the present work [21]. The source terms of Eq. (6b) and Eq. (7) are given by Eq. (9a) and (9b) [24], where n is the total number of neighboring cells occupied by active sites and Δ is the length of a computational cell.

Oxygen diffusion in the pores (3)

$$\nabla \cdot (D_{O_2} \nabla C_{O_2}) = 0 \quad (3a)$$

$$D_{O_2,b}\left(m^2 s^{-1}\right) = 0.22 \times 10^{-4} \frac{(T/293.2K)^{1.5}}{p/1atm} \quad (3b)[43]$$

$$D_{O_2,Kn}\left(m^2 s^{-1}\right) = \frac{d_p(m)}{3}\sqrt{\frac{8RT}{\pi M_{O_2}\left(Kg\ mol^{-1}\right)}} \quad (3c)[44]$$

$$D_{O_2}\left(m^2 s^{-1}\right) = \left(\frac{1}{D_{O_2,Kn}} + \frac{1}{D_{O_2,b}}\right)^{-1} \quad (3d)[45]$$

At the pore-ionomer interface (4)

$$C_{O_2,e} = \frac{C_{O_2}RT}{H} \quad (4a)$$

$$H(\text{Pa m}^3\text{mol}^{-1}) = 1.01325 \times 10^{-1}\exp(-666/T + 14.1) \quad (4b)[46]$$

Oxygen diffusion in the ionomer (5)

$$\nabla \cdot (D_{O_2,e}\nabla C_{O_2,e}) = S_{O_2,e} \quad (5a)$$

$$D_{O_2,e}(\text{m}^2\text{s}^{-1}) = 10^{-10} \times (0.1543(T - 273) - 1.65) \quad (5b)\ [23]$$

Hypothetical oxygen transport equation (6)

$$\nabla \cdot (D_{O_2,e}\nabla C_{O_2}) = \frac{H}{RT}S_{O_2,e} \quad (6a)$$

$$\nabla \cdot (D\nabla C_{O_2}) = S_{O_2} \quad (6b)$$

Proton conduction in the electrolyte

$$\nabla \cdot (\sigma\nabla\varphi_e) = S_e \quad (7)$$

ORR reaction rate

$$i = i_{0,m}\frac{C_{O_2,e}}{C_{O_2,ref}}\exp\left(\frac{\alpha F}{RT}\varphi_e\right) \quad (8)$$

Source term (9)

$$S_{O_2} = \begin{cases} \frac{H}{RT}\frac{n}{\Delta}\frac{i}{4F} & \text{in an active ionomer cell} \\ 0 & \text{others} \end{cases} \quad (9a)$$

$$S_e = \begin{cases} \frac{n}{\Delta} i & \text{in an active ionomer cell} \\ 0 & \text{others} \end{cases} \quad (9b)$$

3.2. Boundary conditions

For predicting oxygen effective diffusivity, constant concentrations are specified at the left (GDL/CL interface) and right boundaries (some distance from the GDL/CL interface into the CL); for the other two directions, namely y and z directions, periodic boundary conditions are employed. The effective diffusivity D_{eff} along the x direction is calculated by

$$D_{\text{eff}} = \frac{\left(\int_0^{L_y}\int_0^{L_z}\left(D\frac{\partial C}{\partial x}\right)\Big|_{L_x} dydz\right)/L_yL_z}{(C_{\text{in}} - C_{\text{out}})/L_x} \quad (10)$$

where C_{in} and C_{out} are the inlet and outlet concentrations, respectively. L_x, L_y and L_z are the size of the domain in the x, y and z directions, respectively. $|_{L_x}$ indicates a local value at $x = L_x$. For predicting proton effective conductivity, the same boundary conditions can be applied and the effective conductivity of protons can be calculated using an equation similar to Eq. (10).

In addition to the diffusion properties discussed above, electrochemical reaction processes within the CL are also investigated. The CL structure constructed here is considered to be adjacent to the GDL/CL interface. As reported in [40], for a 3 μm thick CL, the overpotential drop across the CL is just 0.02 V at a current density of 0.47 A cm^{-2}. In Ref. [23], a potential drop of 0.008 V is considered across the porous CL. Our simulations considering oxygen transfer, proton conduction, and electrochemical reactions, with the same boundary conditions adopted in [20,40], show that the overpotential drop across the 3 μm thick CL shown in Fig. 4 is about 0.0118 V at a current density of 0.858 A cm^{-2}. We find that fully resolving all the coupled processes in the complicated structures shown in Fig. 4 is computationally very expensive. Based on this expense and the relatively small shifts in overpotential calculated, assuming a uniform distribution of ionomer potential in the entire CL is reasonable and practical. In the present study, for the coupled electrochemical reaction and transport processes, the transfer of protons in the ionomer is not solved and the potential in the entire CL is fixed at a given value. At the GDL/CL interface, one layer of pore-only cells is added as the reactant gas reservoir. The boundary conditions for oxygen transport are as follows:

$$\text{at the right boundary}: \frac{\partial C_{O_2}}{\partial x} = 0 \quad (11a)$$

$$\text{at the left boundary}: C_{O_2} = C_{O_2,\text{GDL/CL}} \quad (11b)$$

For the other two directions, namely y and z directions, periodic boundary conditions are employed.

4. Numerical methods

Different numerical methods have been adopted for pore-scale investigations of electrochemical processes in CLs [20–28,40]. Due to its excellent numerical stability and constitutive versatility, the LBM has developed as a promising numerical approach for simulating fluid flow and transport processes, and is particularly successful in applications involving interfacial dynamics and complex geometries, e.g. multiphase flows in porous media [47–49]. In the LBM, instead of directly solving the partial differential equations Eqs. (3a)–(9b), the evolution equations for distribution functions are solved on regular lattices. Variables such as concentration, potential etc. can be calculated by the summation of the distribution functions in all lattice directions [47]. To the best of our knowledge, only Kim and and Pitsch [22] and Wu and Jiang [32] have employed the LBM to investigate diffusion processes in CLs. In both studies, however, only transport processes were investigated while electrochemical reaction processes were not taken into account [22]. In this work, for the first time, the LBM is adopted to simulate the electrochemical processes (both reaction and transport) in a CL under PEMFC cathode conditions. The evolution equation for the concentration distribution function is as follows

$$g_i(x + c_i\Delta t, t + \Delta t) - g_i(x, t) = -\frac{1}{\tau_g}(g_i(x, t) - g_i^{\text{eq}}(x, t)) + a_iS_{O_2}\Delta t \quad (12)$$

where g_i is the distribution function with velocity c_i at the lattice site $\mathbf{x}$ and time t. It is worth mentioning that for simple geometries, a D3Q7 (3 dimensional 7 lattice directions) lattice model (or D2Q5 model in 2D) is sufficient to accurately predict the diffusion process and properties, which can greatly reduce the computational resources, compared with D3Q19 (or D2Q9 in 2D), as proven by our previous work [29,33,34,50–53]. For complex porous structures, especially for those with relatively low porosity such as CL, using a reduced lattice model will damage the connectivity of certain phases, thus leading to underestimated effective transport properties. Therefore, the D3Q19 lattice model (shown in Fig. 3) is

adopted and the discrete lattice velocity $\mathbf{c}_i$ is given by

$$c_i = \begin{cases} 0i = 0 \\ (\pm1,0,0),(0,\pm1,0),(0,\pm1,0)i = 1 \sim 6 \\ (\pm1,\pm1,0),(0,\pm1,\pm1),(\pm1,0,\pm1)i = 7-18 \end{cases} \quad (13)$$

The equilibrium distribution function g^{eq} is defined

$$g_i^{eq} = C_{O_2}/a_i, a_i = \begin{cases} 1/3i = 0 \\ 1/18i = 1 \sim 6 \\ 1/36i = 7-18 \end{cases} \quad (14)$$

The concentration and the diffusivity are obtained by

$$C_{O_2} = \sum g_i, D = \frac{1}{3}(\tau_g - 0.5)\frac{\Delta x^2}{\Delta t} \quad (15)$$

Eqs. (12) and (14) can be proved to recover Eq. (6b) using the Chapman–Enskog expansion.

For proton transfer in the ionomer, a potential distribution function h using the D3Q19 lattice model is adopted. The evolution equation, the equilibrium distribution functions, and the relationship between collision time and proton conductivity for proton transport are similar to those used for oxygen concentration distribution functions. The related expressions are not repeated here for brevity [33].

Our code is parallelized based on domain decomposition using Message Passing Interface (MPI). For predicting effective transport properties, the entire domain is divided into 20, 4 and 4 subdomains in the x, y and z directions, respectively, leading to 320CPU cores used. The running time for proton conduction and oxygen diffusion with and without considering Knudsen diffusion is about 2 and 6 hours, respectively.

5. Results and discussion

5.1. Characterization of the CL Structures

Fig. 4(a) shows a 3D representation of the generated CL structures (with ε=0.4) using the methods in Section 2. The size of the domain is $4000 \times 500 \times 500$ nm, discretized by $800 \times 100 \times 100$ cells with a resolution of 5 nm per cell. For the Pt CL, the volume fractions of carbon, Pt and ionomer calculated using Eq. (1) are 38.12%, 1.28% and 20.59%, respectively. The ionomer-to-carbon weight ratio (I/C ratio) is 0.60. The corresponding Pt loading calculated using Eq. (2) with CL thickness of 4 μm is 0.11 mg cm^{-2}. The carbon and ionomer loading are 0.274 and 0.165 mg cm^{-2}, respectively. As mentioned above, the size of a Pt nanopaticle is 5 nm, indicating a Pt particle can completely occupy a computational cell. In the generated structures shown in Fig. 4, there are a total of 104,443 Pt nanoparticles. Fig. 4(b) shows the detailed distributions of carbon black (top), C/Pt (middle) and ionomer on C/Pt (bottom) for $200 < x < 500$ (lattice units) at z=250 (lattice units). The nonuniform coverage of ionomer on the surface of C/Pt can be clearly observed. For application to the NPMC PANI-FeCo-C CL, the generated structure has a catalyst loading of 0.283 mg cm^{-2}, based on an assumed solid density of 1800 mg cm^{-3}.

The characteristics of the CL nanostructures, including pore size distribution (PSD), specific surface area, and connectivity of different phases dictate the transport properties and reactive processes in the CL. PSD is an important structural characteristic of porous media. Determining the pore size of each pore cell is also required for calculating the Knudsen diffusivity, as shown in Eq. (3c). The 13 direction averaging method proposed in Ref. [23] is adopted to calculate the pore size of each pore cell. Fig. 5 shows the PSD of the reconstructed CL shown in Fig. 4. Using systematic nitrogen adsorption method, it was found that two local peaks of the relative volume can be found, with one below 5 nm and another at around 50∼60 nm, indicating that PSD of CL is bimodal [54]. Since the resolution of one cell in the present work is 5 nm, it is impossible to capture the peak below 5 nm, leading to unimodal distributions as shown in Fig. 5. The maximum pore size is located at around 50 nm, in good agreement with the experimental results [54]. The sizes of all pores are in the range of 5–130 nm, representing the nanoscale characteristics of the CL.

The total surface area and the total volume of the carbon phase are 2,782,840 $(\delta x)^2$ and 3,230,161 $(\delta x)^3$, respectively. The determination of the specific surface area obviously depends on the cell resolution δx, and lower δx leads to higher specific surface area. With δx = 5 nm the specific surface area is 86.2 m^2 g^{-1} for the CL shown in Fig. 4. This value is lower than the experimental results in [54], where the specific surface area for Ketjen Black carbon and Vulcan XC-72 are 890 ± 64.3 m^2 g^{-1} and 228 ± 3.57 m^{2}g^{-1}. Failure to capture pores smaller than 5 nm is a possible reason for the underestimated specific surface area in the present study. As reported in Ref. [54], pores with size smaller than 2 nm constitute ∼25% of the total pore volumes of Ketjen Black carbon.

Connectivity of each phase strongly affects the transport properties as well as the effective active sites. In CL, electrochemical reaction only takes place at active sites neighboring pore, solid phase, and ionomer cells capable of providing oxygen, electrons, and protons, respectively to the sites. This requires that these neighboring cells belong to a continuous percolated path throughout the entire CL, thus being active for reactant transport.

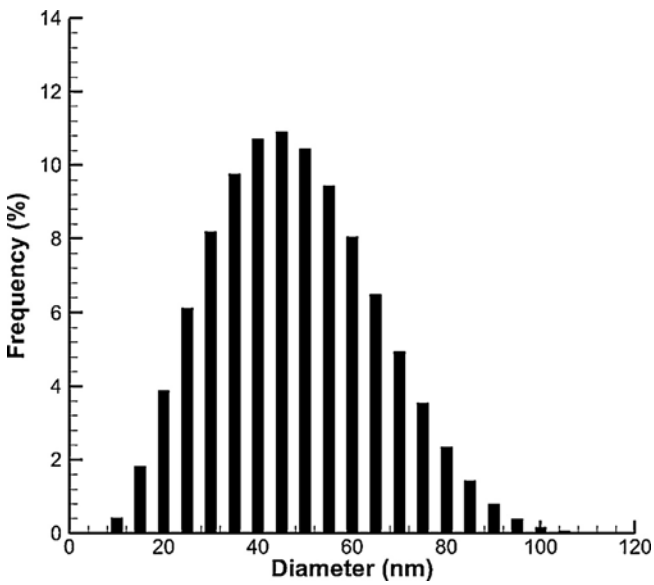

Fig. 5. Pore size distribution of the reconstructed CL structure.

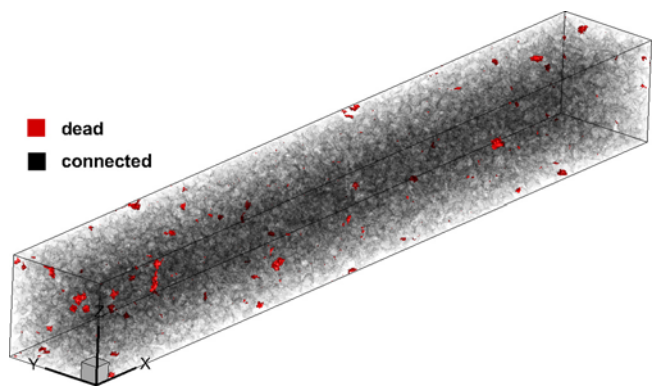

Fig. 6. The "transport" and "dead" portions of solid phase in the reconstructed CL.

It is obvious that if a portion of a certain phase does not penetrate the entire CL, the corresponding phase entering the CL from one end of the CL cannot arrive at the other end through this portion, and this portion is inactive for reactant transport [21]. To identify the active and inactive transport portions in CL, the connectivity of a certain phase needs to be determined. A connected phase labeling algorithm [55] is employed to identify the active and inactive transport portions and to count the number of cells in each portion. This algorithm scans the entire domain, checks the connectivity of a cell with its neighboring 26 points, labels the cell depending on the local connectivity, and finally assigns any portion a distinct label if it is disconnected from other portions. For more details one can refer to Ref. [55]. Fig. 6 shows the solid phase after labeling. The active portion is marked in black, while the inactive portions are in red. The results show that there are 443 portions of solid phase in the reconstructed CL, with one of them as active and the remaining 432 as inactive. The active portion occupies most of the solid phase, with a volume fraction of 99.80% (3,328,017 cells out of the total 3,334,604 solid cells), as clearly seen in Fig. 6 where the inactive portions are shown to be small, discrete sections. For the void phase, there are 536 total void cells in the domain with one active portion and 535 inactive portions. The volume fraction of the active portion is 99.69% (2,892,039 cells of out of the total 2,901,053 void cells). For the ionomer, 793 ionomer cells exist in the domain with one active portion and 792 inactive portions. The volume fraction of the active portion is 99.86% (1,761,838 cells out of the total 1,764,343 ionomer cells). Connectivity analysis of a reconstructed CL based on SEM image in a recent experiment revealed that 99.8% of the solid phase and 99.9% of the void phase are active for transport [37]. Our results are in good agreement with these experimental results. The connectivity of ionomer in Ref. [37] was not reported as SEM cannot distinguish the solid phase and ionomer. The highly transport active characteristics of the different phases in the present study are a result of Step 2a of the QSGS generation in Section 2.1.1.

5.2. Effective diffusivity

Our code is validated by predicting the effective diffusivity of oxygen in a cubic domain containing a sphere whose diameter is the same as the side length of the cube [23]. 200 * 200*200 lattices are employed and the predicted effective diffusivity (normalized by the bulk diffusivity) is 0.3317, in good agreement with the results reported in Ref. [23]. As mentioned previously, for the first study, carbon nanostructures of the NPMC and Pt CLs are kept fixed in order to focus on the effect of active site distribution. Thus, we discuss simulation results in the framework of the Pt CL and compare our predicted values with existing studies centering on Pt CL in the literature and later compare with NPMC CLs.

Fig. 7(a) shows the variations of effective oxygen diffusivity with porosity. In Fig. 7, the effective diffusivity has been normalized by the bulk diffusivity D_b given by Eq. (3b). As the porosity increases, the volume fractions of the solid phase and ionomer phase are reduced. Therefore, it is expected that as the porosity rises, effective diffusivity of oxygen increases and effective conductivity of protons decreases, as shown in Fig. 7. The effective diffusivity predicted by Lange et al. [23] are also plotted in Fig. 7(a). It can be observed that the values predicted in the present study are much lower than that of Lange et al. [23]. For example, for the effective diffusivity without considering Knudsen diffusion, at ε=0.4 the value predicted by the present study is 0.104, only about half of that of Lange et al. [23]. The lower effective diffusivity in the present study is exactly due to the nonuniform ionomer distributions generated by the construction algorithms. As shown in Fig. 4(b), the thickness of the ionomer covering the surface of C/Pt is quite nonuniform and the connections of the ionomer

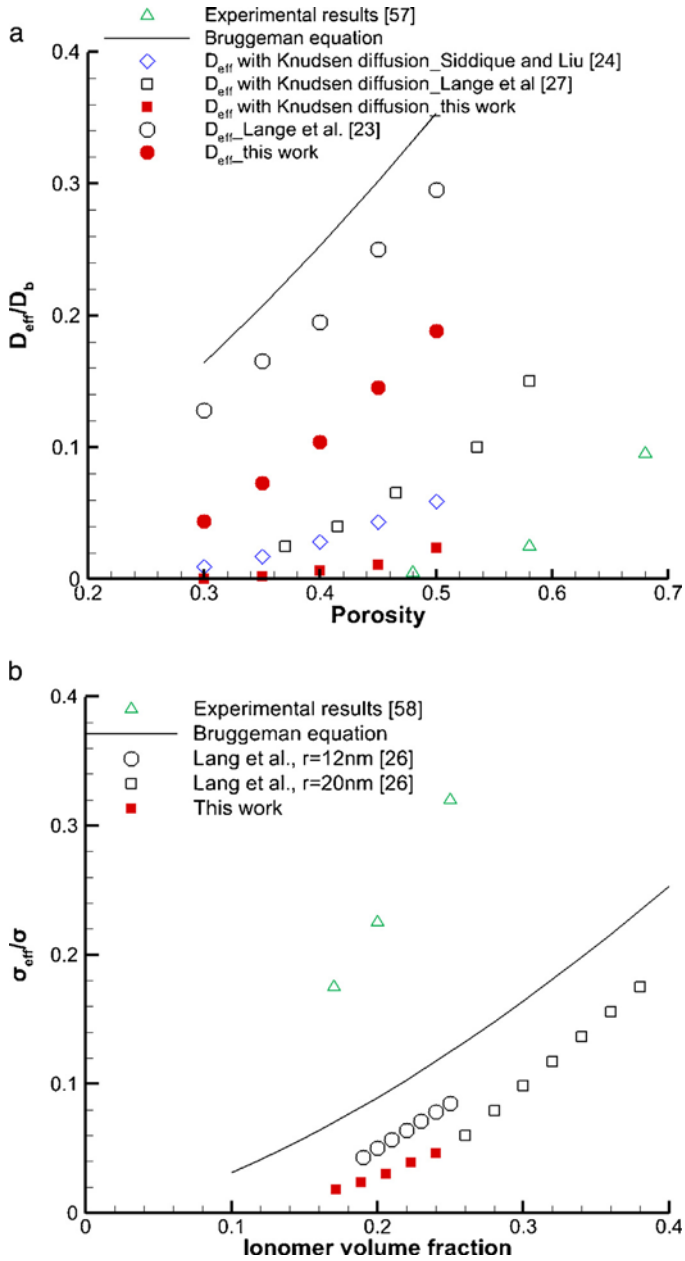

Fig. 7. Macroscopic transport properties obtained from LBM simulations, (a) Effective diffusivity under different porosity; (b) Effective proton conductivity under different ionomer volume fraction.

between different parts of agglomerates even block the void space in some local regions. Such nonuniform distributions and connections greatly increase the tortursity of the pathway for oxygen transport, thus reducing the effective oxygen diffusivity.

Macroscopic models of PEMFCs are highly dependent upon empirical relationship between macroscopic transport properties and statistical structural information of porous components (permeability vs. porosity, diffusivity vs. porosity, etc.) [18]. The Bruggeman equation has been widely used to calculate the effective transport property, Γ, based on porosity:

$$\Gamma_{\text{eff}} = \Gamma\frac{\varepsilon}{\tau} \tag{16}$$

where ε is the volume fraction. τ is the tortuosity of a porous medium, and it is usually set as $\tau = \varepsilon^{-0.5}$, leading to effective transport properties as a pure function of the porosity, namely, $\Gamma_{\text{eff}} = \Gamma\varepsilon^{1.5}$ [18]. Following Eq. (16) and assuming a power

relationship between ε and τ as $\tau = \varepsilon^{\alpha}$, the averaged α for the simulation results of the present work is −1.48, while that of Lange et al. [23] is −0.74 and that of Wu and Jiang is much lower at −2.11 [32]. Based on the above analysis as well as the effective diffusivity predicted by the Bruggeman equation plotted in Fig. 7(a), it can be concluded that the Bruggeman equation greatly overestimates the effective diffusivity, and a lower α should be adopted in the Bruggeman equation to calculate effective diffusivity in CL of PEMFCs [23,24,32]. Very recently, recognizing the much tortuous pathways within the CL, a relationship $\Gamma_{\text{eff}} = \Gamma\varepsilon/\tau^2$ with $\tau = \varepsilon^{-0.5}$ was recommend by Yuan and Sunden [56], leading to $\Gamma_{\text{eff}} = \Gamma\varepsilon^2$.

To the best of our knowledge, only Lange et al. [27], Kim and Pitsch [22], and Siddique and Liu [24] considered the Knudsen diffusion process as well as the nonuniform distributions of the ionomer. Fig. 7(a) displays the results from our simulations as well as that from the literature. Firstly, when Knudsen diffusion is considered, the predicted effective diffusivity is much smaller. This is expected based on Eq. (3d). Under the simulation condition of $T = 333$ K and $P = 1$ atm, the binary diffusivity of oxygen in air is $1.33 \times 10^{-5}\,\text{m}^2\,\text{s}^{-1}$. With a typical pore size of 60 nm, the local Knudsen diffusivity of oxygen is about $9.39 \times 10^{-6}\,\text{m}^2\,\text{s}^{-1}$. Therefore, the total diffusivity in the local pore is $5.50 \times 10^{-6}\,\text{m}^2\,\text{s}^{-1}$, much lower than the bulk diffusivity. Lange et al. [27] compared their results with that of Kim and Pitsch [22]. Both Lange et al. [27] and Kim and Pitsch [22] adopted the sphere-carbon based structures, therefore the effects of structures on the transport properties are similar. Hence only the results of Lange et al. [27] (Fig. 4 in Ref. [27]) are displayed in Fig. 7(a). As shown in Fig. 7(a), both the present study and Siddique and Liu [24] predict lower values than that of Lange et al. [27]. Obviously, different reconstruction methods lead to quite different nanoscale structures of the CL. As mentioned above, the present study and Siddique and Liu [24] adopted the synthesis process based reconstruction method. CL structures reconstructed using the this method (Fig. 2 in [24] and Fig. 4 in the present study) are less regular than that using the sphere-carbon based method (Fig. 1 in Ref. [23]), which is also demonstrated by the tortuosity fits in the previous paragraph, leading to lower effective diffusivity estimated. Therefore, it is apparent that the structures of carbon black play important roles in effective diffusivity. Even with similar reconstruction methods employed, the values of the effective diffusivity predicted by our simulations are smaller than that of Siddique and Liu [24], and our results are closer to the experimental results of Ref. [57]. The discrepancy results from several factors. First, in step 2(a) of the QSGS, if one of the neighboring cells is an ionomer phase cell, the current cell is accepted as an ionomer cell, while in Ref. [24] at least two neighboring cells are required to be ionomer phase for the cell to be assigned to the ionomer phase. Second, the ionomer loading in the present study is 0.3 while that in Ref. [24] is 0.2. Third, a much thicker CL is simulated in the present study. These factors are believed to generate more tortuous void space, resulting in a lower effective diffusivity.

The above discussions indicate that the detailed structures of CL, including the carbon structures as well as the distributions of ionomer, significantly affect the effective diffusivities in CLs [26]. Advanced structure reconstruction algorithms should be adopted to generate nanostructures more closely resembling realistic CLs [24,26]. Process based reconstruction algorithms have proven to be a good choice [24] based on the comparison between the simulation results of the present study and those in the literature. Further, it can be observed from Fig. 7(a) that as the porosity increases, the discrepancy between our simulation results and that from the literature is reduced. For porosity in the range of 0.3–0.50, the effective diffusivity predicted by Siddique and Liu [24] ranges from 0.00927∼0.0587, while that in the present study ranges from 0.000336 to 0.0239. The ratio between their and our work is 27.59 at ε=0.3, but only 2.46 at ε=0.5. This is because Knudsen diffusion is very sensitive to the local pore size which is affected by the local ionomer distributions. Under low porosity, the local pore is quite likely to be blocked by the bridging of ionomer between separated agglomerates. Finally, the simulated values of the effective diffusivity in the present study are still higher than the experimental results [57], and using more accurate relationship between pore diameter and Knudsen diffusivity is believed to be able to further reduce the discrepancy between simulation and experimental results [27].

5.3. Effective conductivity of proton

Fig. 7(b) shows the predicted effective proton conductivity of the present study as well as experimental and numerical results from the literature [26,58]. The value of the effective conductivity from our work is very close to that calculated by Lange et al. [26] with carbon sphere diameter $r = 20$ nm and is lower than that calculated with $r = 12$ nm. The reconstruction algorithm in the present study generates nonuniform distributions of ionomer. On one hand, the nonuniform distributions can improve the connection of ionomer between different solid phase agglomerates, reducing the tortuosity of the proton path and thus helping to increase the effective conductivity. On the other hand, however, extremely thin ionomer films on the surface of the C/Pt act as barriers for proton transport, as shown in Fig. 4(b). Compared with the simulation results in Ref. [26], it can be seen that the nonuniform distributions of ionomer does not increase the proton conductivity, indicating the offset of positive and negative effects. In addition, for solely considering proton transport in ionomer, again the Bruggeman equation overestimates the effective conductivity, just as its performance for predicting effective diffusivity of oxygen, because it underestimates the tortuosity. Further, both this work and Ref. [26] as well as the Bruggeman equation predict much lower values of the effective conductivity than the experimental results [58]. This indicates that there are potentially other mechanisms for proton transport in CL [26]. When a PEMFC is operated under high current density, liquid water is generated in the cathode CL which can increase the water content of ionomer and fill the void pores. Ionomer with high water content provides high proton conductivity. In addition, protons can directly transport in the liquid water [59]. Therefore, effective conductivity of protons not only depends on the ionomer content and distribution, but also is affected by the operating humidity conditions [58].

5.4. Reactive transport process

The current balance for the cathode CL can be written as

$$\int_S i_0 \frac{C_{O_2,e}}{C_{O_2,ref}} \exp\left(-\frac{\alpha F}{RT}\eta\right) ds = i_d . A_{cross} \tag{17}$$

where A_{cross} is the cross-sectional area of CL and i_d is the discharge current density applied on A_{cross}. The left hand side of Eq. (17) is the integration of the current density over all the active sites, with S denoting the interfacial surface. Assuming an averaged oxygen concentration and overpotenial over the entire CL, Eq. (17) can be modified as [20]

$$i_0 \frac{\overline{C_{O_2,e}}}{C_{O_2,ref}} \exp\left(-\frac{\alpha F}{RT}\overline{\eta}\right) . \frac{A_{reaction}}{A_{cross}} = i_d \tag{18}$$

where $A_{reaction}$ is the total active surface within the cathode CL. It can be concluded from Eq. (18) that for increasing i_d, one can increase the total reactive surface area $A_{reaction}$, increase the

Table 1
Parameter values used in the simulation

Parameters	Value	
Temperature	T	333 K
Pressure	P	1.5 bar
Reference oxygen concentration	$C_{O2,ref}$	40.96 $m^3\,mol^{-1}$
cathode transfer coefficient	α	0.61
modified exchange current density	$i_{0,m}$	0.01 $A\,m^{-2}$
Ionomer potential	ϕ_e	0.6 V
Oxygen concentration at GDL/CL interface	$C_{O2,ref}$	10.28 $m^3\,mol^{-1}$

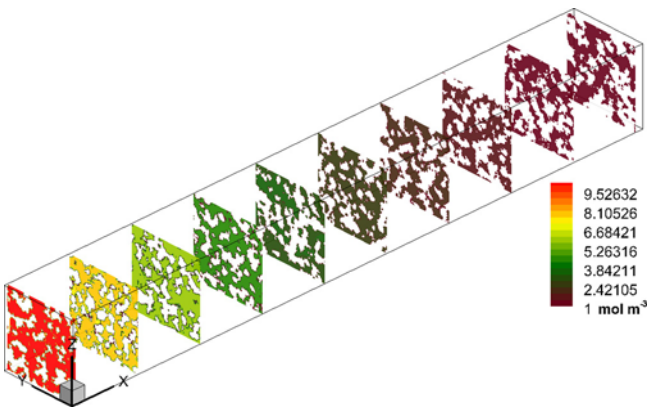

Fig. 8. Oxygen concentration in the NPMC CL.

reaction rate (by increasing i_0), or enhance the mass transport to increase $\overline{C_{O_2,e}}$. Compared with the Pt CL where only the sites with Pt nanoparticles are active, the PANI-FeCo-C CL has an assumed uniform distributions of actives sites on the entire surface of solid phase [11], therefore the entire solid surface is reactive. Consequently, $A_{reaction}$ of the PANI-FeCo-C CL is much higher than that of Pt CL; and for the reconstructed structure shown in Fig. 4, $A_{reaction,NPMC}/A_{reaction,Pt}$ is 7.44. However, the reaction rate for the NPMC CL is much lower than that of Pt CL [11], typically two orders of magnitude lower. In the present study, $i_{0,m}$ in Eq. (8) for PANI-FeCo-C is set as 1/100 of that of Pt [11]. Using the physicochemical model established in Section 3 and the LBM in Section 4, reactive transport in Pt CL and PANI-FeCo-C CL is simulated. The parameters used in the simulations are listed in Table 1. One such simulation takes about 8 hours to converge using 4000CPU cores.

The oxygen concentration field in the NPMC predicted by the LBM simulations is displayed in Fig. 8, with electrolyte potential ϕ_e in the domain as 0.6 V, which is a good value for studying both kinetic loss and mass transport limitations [5]. As shown Fig. 8, the distributions are rather complicated due to the complex nanoscale structures. The oxygen concentration continuously declines from the left inlet to the outlet, due to the electrochemical reactions. Figs. 9 and 10 show the oxygen concentration and oxygen reaction rate along the x direction. Comparing the NPMC CL with the Pt CL, it can be seen that although the total reaction surface area of NPMC CL is seven times larger than that of Pt CL, the reaction rate within the NPMC CL is much lower, due to the much lower i_0. As discussed in Section 2, the catalyst loading for the NPMC CL studied in the present study is only 0.283 $mg\,cm^{-2}$, while in literature it is reported that a 1–5 $mg\,cm^{-2}$ loading can be applied. The higher loading can be achieved by adopting a thicker CL. Certainly, using a thicker NPMC CL would mean the unconsumed oxygen shown in Fig. 9 can be further utilized and the current density will increase. However, a thicker NPMC will lead to higher mass transport resistance for oxygen to arrive at the active sites near the CL/PEM interface, especially at high current density [5].

An important synthesis step for making PANI-FeCo-C catalysts is acid leaching which can remove inactive surface species, leading to improved active-site densities and increased micropores (with pore size of a few nanometers) [11]. The dominant diffusion mechanism in such micro-pores is Knudsen diffusion, which is much slower than the bulk diffusion in meso or macropores (~few tens of nanometers) [10,23]. In the present study, micropores and mesopores are artificially generated within the solid phase using QSGS to investigate their effects on transport processes and electrochemical reactions. Note that these pores are only generated inside the solid phase, while the shell of the solid phase is not changed, without disrupting the

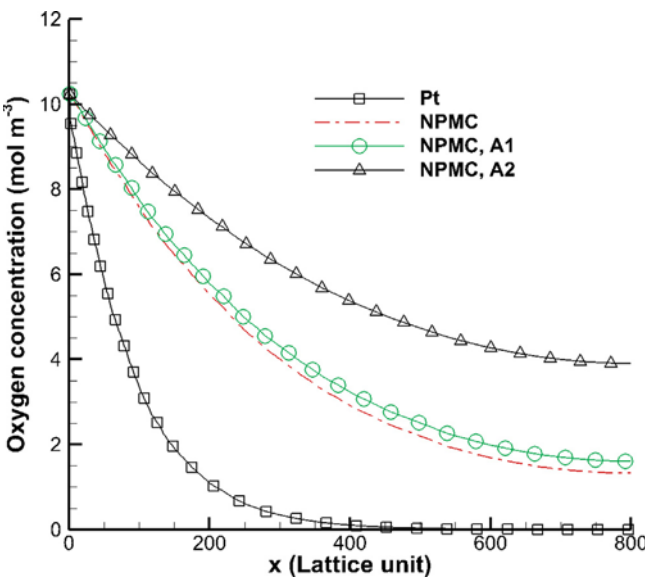

Fig. 9. Distribution of oxygen concentration along ***x*** direction.

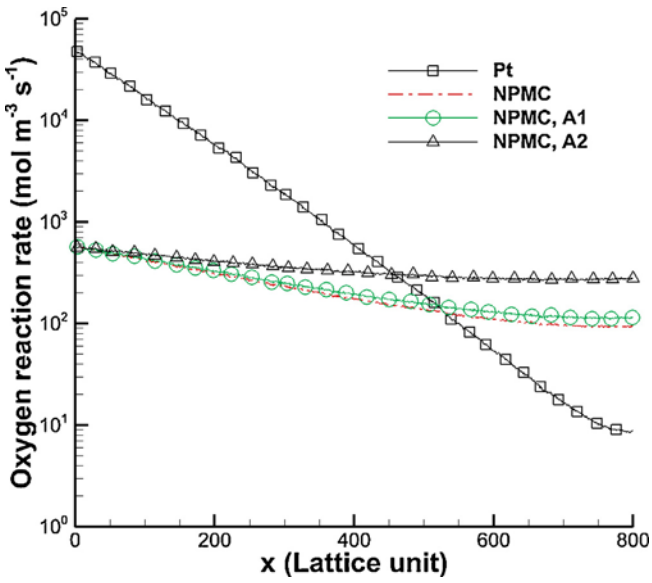

Fig. 10. Distribution of reaction rate along ***x*** direction.

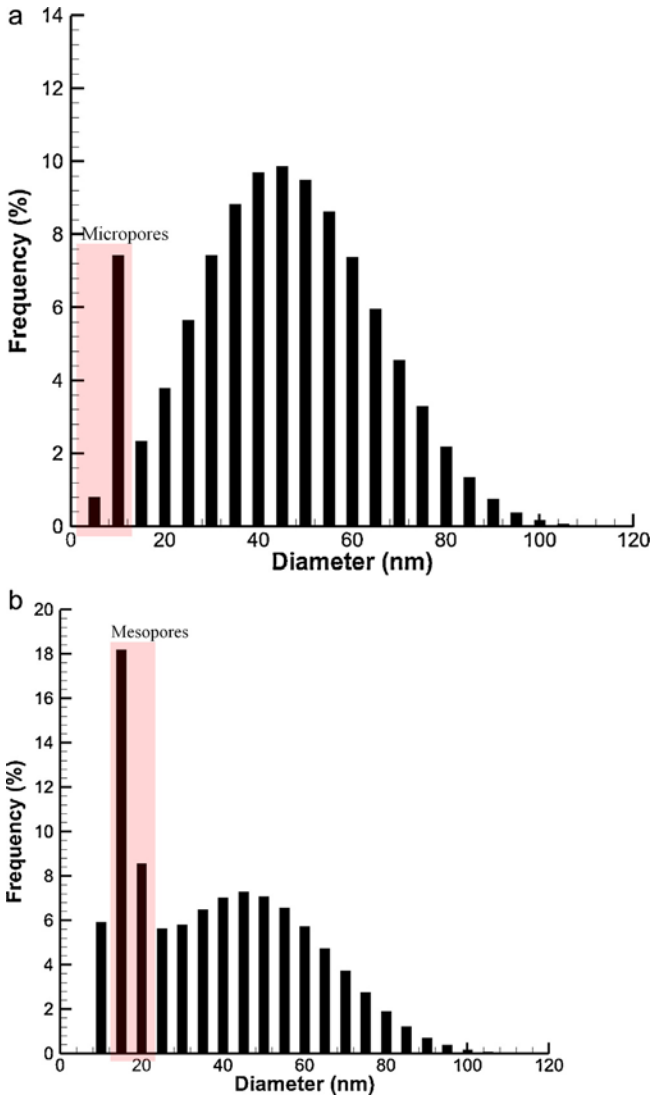

Fig. 11. Pore size distribution for NPMC with micropores and mesopores generated, (a) NPMC A1, micropores generated; (b) NPMC A2, mesopores generated.

contact between solid phase and ionomer. To focus on the effects of these pores on mass transport, the distributions of ionomer are not changed, meaning that there is no ionomer within these newly generated pores where electrochemical reactions are hence not allowed. Two structures called NPMC A1 and NPMC A2 are generated, and their PSDs are shown in Fig. 11(a) and (b), respectively. For NPMC A1, pores with diameter of 5∼10 nm are increased, while for NPMC A2 pores with diameter 15–25 nm are increased, as can be observed from the PSDs. The effective diffusivity for NPMC A1 and NPMC A2 D_{eff}/D_b are 6.76×10^{-3} and 1.98×10^{-2}, respectively. Compared with the original NPMC with $D_{eff}/D_b = 6.45 \times 10^{-3}$, micropores in NPMC A1 contributes little to the mass transport; in contrast, NPMC A2 greatly reduces the mass transport resistance and is expected to improve the cell performance. As shown in Fig. 9 and 10, for NPMC A1, the oxygen concentration at the right outlet increases only 21%, and the oxygen reaction rate is slightly increased. For NPMC A2, the oxygen concentration at the outlet increases three times, and the reaction rate enhances remarkably. This confirms that due to less efficient Knudsen diffusion within micropores, mesopores or macropores should be generated for the purpose of reducing mass transport limitation in NPMC CL, which is in consistent with the experimental results in Ref. [10].

6. Conclusion

In this study, nanoscale structures of CLs are constructed using the QSGS method [41]. The reconstruction processes follows the experimental fabrication process including carbon seed generation, carbon phase growth, Pt deposition and ionomer coverage [24]. Detailed distributions of Pt, carbon, ionomer and void space are obtained from the reconstruction processes owing to the high resolution of the considered structures. The structures are analyzed for pore size distribution, specific area, and phase connectivity. Macroscopic transport properties of the reconstructed CL are numerically predicted using LBM. The detailed structures of CLs, including the carbon and ionomer distribtuions, significantly affect the effective diffusivities in the CL. The tortuosity predicted is much higher than that commonly used in the Bruggeman equation. In addition, Knudsen diffusion plays a significant role in oxygen diffusion and significantly reduces oxygen's effective diffusivity. The effective proton conductivity predicted is close to the simulation results in the literature [26] and much lower than experimental results [58], indicating other proton transport mechanisms such as proton transport in liquid water [59].

Reactive transport processes in NPMC CLs and Pt CLs are numerically investigated at the nanoscale using the LBM. The simulation results show that although the total reaction surface area of NPMC CL considered in this study is larger than that of the Pt CL, the reaction rate within the NPMC CL is lower than that in Pt CL, due to much smaller reaction rate coefficient. To further improve the performance of the NPMC CL, the reaction surface area needs to be increased to overcome the slow reaction rate coefficient. To improve the microstructure for optimal reaction surface area is a topic of our ongoing study. In addition, the effects of micropores and mesopores on mass transport are studied. It is found that micropores (a few nanometers) contribute little to mass transport. Mesopores (a few tens of nanometers) or macropores are required to increase the mass transport rate.

Acknowledgement

The authors acknowledge the support of LANL's LDRD Program, Institutional Computing Program, National Nature Science Foundation of China (51406145, 51136004 and 51320105004), and China Postdoctoral Science Foundation (2014M550496). Li Chen appreciates the helpful discussions with Doctor Yutong Mu and WenZhen Fang from Xi'an Jiaotong University, China, and Prof. Gregory A. Voth from the University of Chicago, USA.

Reference

[1] A. Arvay, E. Yli-Rantala, C.-H. Liu, X.-H. Peng, P. Koski, L. Cindrella, P. Kauranen, P.M. Wilde, A.M. Kannan, Journal of Power Sources 213 (2012) 317–337.
[2] H.A. Gasteiger, J.E. Panels, S.G. Yan, Journal of Power Sources 127 (2004) 162–171.
[3] H.A. Gasteiger, S.S. Kocha, B. Sompalli, F.T. Wagner, Applied Catalysis B: Environmental 56 (2005) 9–35.
[4] B.D. James, J.A. Kalinoski, Proc. U.S. Department of Energy-Hydrogen Program, 2008 Annual Progress Report, 2008.
[5] F. Jaouen, E. Proietti, M. Lefèvre, R. Chenitz, J.-P. Dodelet, G. Wu, H.T. Chung, C. M. Johnston, P. Zelenay, Energy Environ. Sci. 4 (2011) 114–130.
[6] D.C. Higgins, Z. Chen, The Canadian Journal of Chemical Engineering 91 (2013) 1881–1895.
[7] R. Jasinski, Nature 201 (1964) 1212–1213.
[8] H.A. Gasteiger, N.M. Marković, Science 324 (2009) 48–49.
[9] M. Lefèvre, E. Proietti, F. Jaouen, J.-P. Dodelet, Science 324 (2009) 71–74.
[10] E. Proietti, F. Jaouen, M. Lefèvre, N. Larouche, J. Tian, J. Herranz, J.-P. Dodelet, Nat Commun 2 (2011) 416.
[11] G. Wu, K.L. More, C.M. Johnston, P. Zelenay, Science 332 (2011) 443–447.

[12] S. Gupta, D. Tryk, I. Bae, W. Aldred, E. Yeager, J Appl Electrochem 19 (1989) 19–27.
[13] G. Wu, P. Zelenay, Accounts of Chemical Research 46 (2013) 1878–1889.
[14] G. Wu, M. Nelson, S. Ma, H. Meng, G. Cui, P.K. Shen, Carbon 49 (2011) 3972–3982.
[15] G. Wu, Z. Chen, K. Artyushkova, F.H. Garzon, P. Zelenay, ECS Transactions 16 (2008) 159–170.
[16] F. Jaouen, J.-P. Dodelet, Electrochimica Acta 52 (2007) 5975–5984.
[17] T. Berning, D.M. Lu, N. Djilali, Journal of Power Sources 106 (2002) 284–294.
[18] W.Q. Tao, C.H. Min, X.L. Liu, Y.L. He, B.H. Yin, W. Jiang, Journal of Power Sources 160 (2006) 359–373.
[19] W. Sun, B.A. Peppley, K. Karan, Electrochimica Acta 50 (2005) 3359–3374.
[20] G. Wang, P.P. Mukherjee, C.-Y. Wang, Electrochimica Acta 51 (2006) 3151–3160.
[21] G. Wang, P.P. Mukherjee, C.-Y. Wang, Electrochimica Acta 52 (2007) 6367–6377.
[22] S.H. Kim, H. Pitsch, Journal of The Electrochemical Society 156 (2009) B673–B681.
[23] K.J. Lange, P.-C. Sui, N. Djilali, Journal of the Electrochemical Society 157 (2010) B1434–B1442.
[24] N.A. Siddique, F. Liu, Electrochimica Acta 55 (2010) 5357–5366.
[25] R. Barbosa, J. Andaverde, B. Escobar, U. Cano, Journal of Power Sources 196 (2011) 1248–1257.
[26] K.J. Lange, P.-C. Sui, N. Djilali, Journal of Power Sources 196 (2011) 3195–3203.
[27] K.J. Lange, P.-C. Sui, N. Djilali, Journal of Power Sources 208 (2012) 354–365.
[28] P.P. Mukherjee, C.-Y. Wang, Journal of The Electrochemical Society 153 (2006) A840–A849.
[29] L. Chen, H.-B. Luan, Y.-L. He, W.-Q. Tao, International Journal of Thermal Sciences 51 (2012) 132–144.
[30] J. Park, M. Matsubara, X. Li, Journal of Power Sources 173 (2007) 404–414.
[31] P.P. Mukherjee, C.-Y. Wang, Q. Kang, Electrochimica Acta 54 (2009) 6861–6875.
[32] W. Wu, F. Jiang, International Journal of Hydrogen Energy 39 (2014) 15894–15906.
[33] L. Chen, Y.-L. Feng, C.-X. Song, L. Chen, Y.-L. He, W.-Q. Tao, International Journal of Heat and Mass Transfer 63 (2013) 268–283.
[34] L. Chen, Y.-L. He, Q. Kang, W.-Q. Tao, Journal of Computational Physics 255 (2013) 83–105.
[35] G.R. Molaeimanesh, M.H. Akbari, Journal of Power Sources 258 (2014) 89–97.
[36] P.P. Mukherjee, Q. Kang, C.-Y. Wang, Energy & Environmental Science 4 (2011) 346–369.
[37] S. Thiele, T. Fürstenhaupt, D. Banham, T. Hutzenlaub, V. Birss, C. Ziegler, R. Zengerle, Journal of Power Sources 228 (2013) 185–192.
[38] S. Litster, G. McLean, Journal of Power Sources 130 (2004) 61–76.
[39] V. Nallathambi, J.-W. Lee, S.P. Kumaraguru, G. Wu, B.N. Popov, Journal of Power Sources 183 (2008) 34–42.
[40] J. Zhang, W. Yang, L. Xu, Y. Wang, Electrochimica Acta 56 (2011) 6912–6918.
[41] M. Wang, J. Wang, N. Pan, S. Chen, Phys. Rev. E 75 (2007) 036702.
[42] C.V. Rao, B. Viswanathan, The Journal of Physical Chemistry C 114 (2010) 8661–8667.
[43] E.L. Cussler, Diffusion: mass transfer in fluid systems, third edition, Cambridge University, New York, 1997.
[44] R.E. Cunningham, R.J.J. Williams, Diffusion in gases and porous media, Plenum, New York, 1980.
[45] W.G. Pollard, R.D. Present, Phys. Rev. 73 (1948) 762–774.
[46] D.M. Bernardi, M.W. Verbrugge, J. Electrochem. Soc. 139 (1992) 2477–2491.
[47] S. Chen, G.D. Doolen, Annual Review of Fluid Mechanics 30 (1998) 329–364.
[48] C.K. Aidun, J.R. Clausen, Annual Review of Fluid Mechanics 42 (2010) .
[49] L. Chen, Q. Kang, Y. Mu, Y.-L. He, W.-Q. Tao, International Journal of Heat and Mass Transfer 76 (2014) 210–236.
[50] L. Chen, Q. Kang, Y.-L. He, W.-Q. Tao, Langmuir 28 (2012) 11745–11754.
[51] L. Chen, Q. Kang, Y.-L. He, W.-Q. Tao, International Journal of Hydrogen Energy 37 (2012) 13943.
[52] L. Chen, H. Luan, Y. Feng, C. Song, Y.-L. He, W.-Q. Tao, International Journal of Heat and Mass Transfer 55 (2012) 3834–3848.
[53] L. Chen, Q. Kang, B.A. Robinson, Y.-L. He, W.-Q. Tao, Physical Review E 87 (2013) 043306.
[54] T. Soboleva, X. Zhao, K. Malek, Z. Xie, T. Navessin, S. Holdcroft, ACS Applied Materials & Interfaces 2 (2010) 375–384.
[55] C. Pan, E. Dalla, D. Franzosi, C.T. Miller, Advances in Water Resources 30 (2007) 623–640.
[56] J. Yuan, B. Sundén, International Journal of Heat and Mass Transfer 69 (2014) 358–374.
[57] Z. Yu, R.N. Carter, Journal of Power Sources 195 (2010) 1079–1084.
[58] Y. Liu, M.W. Murphy, D.R. Baker, W. Gu, C. Ji, J. Jorne, H.A. Gasteiger, Journal of The Electrochemical Society 156 (2009) B970–B980.
[59] P. Choi, N.H. Jalani, R. Datta, Journal of The Electrochemical Society 152 (2005) E123–E130.